

Emergence of the *Gaia* Phase Space Spirals from Bending Waves

Keir Darling^{*} and Lawrence M. Widrow[†]

Department of Physics, Engineering Physics & Astronomy, Queen's University, Stirling Hall, Kingston, ON K7L 3N6, Canada

Accepted XXX. Received YYY; in original form ZZZ

ABSTRACT

We discuss the physical mechanism by which pure vertical bending waves in a stellar disc evolve to form phase space spirals similar to those discovered by Antoja et al. in *Gaia* Data Release 2. These spirals are found by projecting Solar Neighbourhood stars onto the $z - v_z$ plane. Faint spirals appear in the number density of stars projected onto the $z - v_z$ plane, which can be explained by a simple model for phase wrapping. More prominent spirals are seen when bins across the $z - v_z$ plane are coloured by median v_R or v_ϕ . We use both toy model and fully self-consistent simulations to show that the spirals develop naturally from vertical bending oscillations of a stellar disc. The underlying physics follows from the observation that the vertical energy of a star (essentially, its “radius” in the $z - v_z$ plane) correlates with its angular momentum or, alternatively, guiding radius. Moreover, at fixed physical radius, the guiding radius determines the azimuthal velocity. Together, these properties imply a link between in-plane and vertical motion that lead directly to the *Gaia* spirals. We show that the cubic $R - z$ coupling term in the effective potential is crucial for understanding the morphology of the spirals. This suggests that phase space spirals might be a powerful probe of the Galactic potential. In addition, we argue that self-gravity is necessary to properly model the evolution of the bending waves and their attendant phase space spirals.

Key words: Galaxy: kinematics and dynamics – Galaxy: structure – Galaxy: disc

1 INTRODUCTION

Gaia Data Release 2 (GDR2) (Gaia Collaboration et al. 2018a), which includes measurements of the six-dimensional phase space coordinates for some seven million stars, has afforded astronomers an unprecedented picture of the local stellar kinematics in our Galaxy (Gaia Collaboration et al. 2018b). Arguably, the most intriguing result from the nascent analysis of this data set has been the discovery of spiral patterns in certain phase space projections of Solar Neighborhood stars by Antoja et al. (2018). They selected stars in a circular arc that spanned 8° in Galactic azimuth ϕ and a range in Galactocentric radius R from 8.24 kpc to 8.44 kpc. They then computed the number density distribution of the ~ 900 k stars within this region as a function z and v_z , the position and velocity in the direction perpendicular to the Galactic midplane. The resulting plot showed a spiral pattern of 1-2 complete wraps within a region of the $z - v_z$ plane extending to ~ 700 pc in $|z|$ and ~ 40 km s⁻¹ in $|v_z|$. More prominent spirals appeared when they “coloured” the

$z - v_z$ plane by median v_R and v_ϕ . Antoja et al. (2018) interpreted the spirals as a telltale sign of phase wrapping and were able to explain their general morphology by a simple model for the local gravitational potential.

In this paper, we delve deeper into the physics of the “*Gaia* spirals”. Our hypothesis is that a pure bending wave naturally evolves to form spiral patterns in the (z, v_z, v_ϕ, v_R) phase space. (For a different take on some of the same ideas, see Binney & Schoenrich (2018).) Bending waves are a natural feature of disc galaxies. The most conspicuous examples are the warps seen in edge-on galaxies (See Binney (1992) and Sellwood (2013) for reviews of galactic warps.). These warps amount to a bending of both HI and stellar discs from the midplane by $\sim 1 - 3$ kpc. Recently, Xu et al. (2015) found asymmetries in the number counts of stars above and below the disc at Galactocentric radii between 12 kpc and 18 kpc, which they interpreted as evidence for ripples or corrugations in the disc. In addition, Schönrich & Dehnen (2018) found wavelike patterns in the mean vertical motion of Solar Neighbourhood stars as a function of L_z , the angular momentum about the rotation axis of the Galaxy. Since L_z is roughly proportional to guiding radius (at least, where the rotation curve is approximately flat)

^{*} E-mail: 13kd39@queensu.ca

[†] E-mail: widrow@queensu.ca

these velocity ripples may well be the velocity counterpart to those seen in number counts (Chequers et al. 2018). Further evidence for bending and breathing modes has been seen in both number counts and bulk motions of Solar Neighbourhood stars (see, for example, Widrow et al. (2012); Williams et al. (2013); Carlin et al. (2013); Yanny & Gardner (2013); Gaia Collaboration et al. (2018a); Bennett & Bovy (2018)). They can be excited by a passing satellite (Widrow et al. 2012; Feldmann & Spolyar 2015; Gómez et al. 2013, 2017), spiral structure or the bar (Debattista 2014; Monari et al. 2015), or even shot noise in an N-body simulation (Chequers & Widrow 2017).

In this paper we sidestep the issue of what perturbs the disc by imposing an initial *ad hoc* vertical perturbation. The excitation of bending and breathing waves due to a passing satellite is discussed in detail by Widrow et al. (2014) and demonstrated in N-body simulations of both isolated discs in discs in fully cosmological simulations by Gómez et al. (2013); Feldmann & Spolyar (2015); Gómez et al. (2017); Chequers et al. (2018). In essence, these excitations are the early stages of the disc-heating events discussed in Toth & Ostriker (1992) and Sellwood et al. (1998). The excitation of perturbations in the context of phase space spirals using the impulse approximation is discussed in Binney & Schoenrich (2018).

In Section 2 we consider a series of toy-model simulations where test particles are evolved in time-dependent, axisymmetric potentials. These simulations allow us to illustrate the essential physics of phase space spirals and, in particular, highlight the importance of the non-separable nature of the effective potential for disc stars. In Section 3, we then demonstrate the link between bending waves and phase space spirals in a fully self-consistent disc-bulge-halo model of the Milky Way using standard N-body methods. We conclude in Section 4 with a summary of our results and suggestions for further investigations of these ideas.

2 KINEMATIC SPIRALS

2.1 Distribution Function

Consider a distribution of test particles in a time-independent, axisymmetric potential $\Phi(R, z)$. All particle orbits admit two integrals of motion: the angular momentum about the symmetry axis $L_z = Rv_\phi$ and the total energy $E = \frac{1}{2}v^2 + \Phi(R, z)$. If the potential is an additively separable function, that is, if it can be written in form

$$\Phi(R, z) = \psi(R) + \chi(z), \quad (1)$$

then the vertical energy

$$E_z = \frac{1}{2}v_z^2 + \Phi(R, z) - \Phi(R, 0) \quad (2)$$

is also an integral of motion. In this case, it is convenient to define the planar energy $E_p = E - E_z$. Even if the potential cannot be written in the form given by Eq. 1, the vertical energy is approximately conserved for particles on nearly circular orbits (Binney & Tremaine 2008).

Analytic functions of E_p , E_z , and L_z can be used as the building blocks for a disc that is close to equilibrium.

Following Kuijken & Dubinski (1995) we consider the quasi-isothermal distribution function (DF)

$$f(E_z, E_p, L_z) = \frac{g}{\sigma_z \sigma_R^2} \exp \left[-\frac{E_p - E_c}{\sigma_R^2} - \frac{E_z}{\sigma_z^2} \right] \quad (3)$$

where E_c is the energy of a particle on a circular orbit with angular momentum L_z , and g , σ_R , σ_z , and E_c are functions of L_z .

The function $g(L_z)$ determines the radial profile of the surface density, which is obtained by integrating the DF over velocities and z . Furthermore, the guiding radius R_c for a particle on a circular orbit is an implicit function of L_z . Thus, we can use R_c , which is an integral of motion, as a proxy for radius R when constructing the DF. For example, an exponential disc is obtained by choosing $g \propto \exp(-R_c/R_d)$.

Our interest here is in stars in the Solar Neighbourhood. We are therefore led to consider the idealized case where

$$g(L_z) \propto \delta(L_z - L_{z0}). \quad (4)$$

The density is then given by

$$\rho(R, z) \propto \exp \left[-\frac{\Phi_{\text{eff}}(R, 0) - E_c}{\sigma_R^2} - \frac{\Phi_z(R, z)}{\sigma_z^2} \right] \quad (5)$$

where $\Phi_{\text{eff}}(R) = \Phi(R, 0) + L_{z0}^2/2R^2$ is the effective potential for a particle with angular momentum L_{z0} and $\Phi_z(R, z) \equiv \Phi(R, z) - \Phi(R, 0)$. Note that the peak of the radial distribution of particles coincides with the minimum of the effective potential, that is, the guiding radius of a particle with angular momentum L_{z0} . The main advantage of this DF is that it is easily sampled. It is, however, too simplistic for our purposes as we now describe.

In the DF given by Eq. 3, the angular momentum determines a particle's guiding radius and hence the probability distribution functions for a particle's phase space coordinates R , z , v_R , v_ϕ , and v_z . If we introduce a bending perturbation to this DF, that is, if we displace the DF in either z or v_z , then the distribution will phase wrap in the $z - v_z$ plane producing a spiral pattern similar to the one seen in the number counts. However, since the DF is separable in $z - v_z$ and $R - v_R - v_\phi$, spiral patterns will not appear when the $z - v_z$ plane is coloured by median v_R or v_ϕ .

Of course, in a real galaxy one has a distribution of stars in L_z at a given R . To mimic this effect while retaining the simplicity of Eq. 4 we consider a superposition of two delta-function distributions,

$$g(L_z) = \alpha_1 \delta(L_z - L_{z1}) + \alpha_2 \delta(L_z - L_{z2}), \quad (6)$$

which we refer to as populations 1 and 2. In what follows, we assume that $\alpha_1 = \alpha_2 = 0.5$ and choose L_{z1} and L_{z2} so that the two guiding radii are 7.41 kpc and 7.94 kpc, respectively. Furthermore, we assume that σ_R and σ_z are given by

$$\begin{aligned} \sigma_R(R_c) &= \sigma_{R,0} e^{-(R_c - R_s)/2R_d} \\ \sigma_z(R_c) &= \sigma_{z,0} e^{-(R_c - R_s)/2R_d} \end{aligned} \quad (7)$$

with $R_d = 2.1$ kpc, $\sigma_{R,0} = 26$ km s⁻¹, and $\sigma_{z,0} = 16$ km s⁻¹.

2.2 $R - z$ Coupling in the Potential

In this section we consider a toy model potential that allows us to isolate the effect $R - z$ coupling terms in the effective potential have on phase space spirals. Recall that in the epicycle approximation (Binney & Tremaine 2008) one expands the effective potential to terms quadratic in $R - R_c$ and z . To the extent that the approximation holds, stars execute simple harmonic motion in R and z . Of course, without the higher order terms in the potential, all stars would orbit in the $z - v_z$ plane at the same frequency and phase space spirals would never develop.

As discussed above, the vertical energy E_z is conserved so long as the potential is additively separable. We first consider a model for the potential that is additively separable but includes higher order terms in z and $R - R_c$. As we'll see, spirals appear in this model but lack many of the qualitative features seen in the data. We then augment this model with an $(R - R_c)z^2$ term. This term, along with an $(R - R_c)^3$ term, are the leading corrections to the epicycle approximation. The spirals in this case have a richer phenomenology than the ones in our separable model and share many of the features with the spirals seen in *Gaia* DR2.

2.2.1 kinematic spirals in an additively separable potential

Consider an additively separable potential given by Eq. 1 with

$$\chi(z) = ab^2 \sqrt{\frac{z^2}{b^2} + 1} + cz^2 \quad (8)$$

and

$$\psi(R) = \frac{v_o^2}{2} \ln(R^2 + R_o^2). \quad (9)$$

The form of the vertical potential χ is similar to that from the Oort problem analysis of Kuijken & Gilmore (1989) while ψ is the logarithmic potential (see, for example, Binney & Tremaine (2008)), which gives a flat rotation curve for $R \gg R_o$. In what follows we choose $a = 0.07 \text{ Myr}^{-2}$, $b = 23 \text{ pc}$ and $c = 0.006 \text{ Myr}^{-2}$, which give a vertical potential consistent with models for the vertical potential in the Solar Neighborhood (See Widrow et al. (2014)). We also choose $v_o = 217 \text{ km s}^{-1}$ and $R_o = 6.1 \text{ kpc}$ to give a radial potential consistent with the realistic Milky Way model considered in Section 2.3.

We next sample the DF for 500k particles. Properties of the initial conditions are exhibited in Fig. 1 and 2. The top panel of Fig. 1 shows the number density of stars as a function of Galactocentric radius for the two distributions. Evidently, the model has the desired property that the distribution of stars at a given radius comprises an admixture from the two L_z populations. The bottom panel shows the distribution of stars as a function of R and v_ϕ . Since $v_\phi = L_z/R$, the distribution at a given radius is essentially the sum of two delta functions with population 1 stars having a lower azimuthal velocity than the population 2 stars at the same R . Finally, in the middle panel, we show the distribution in R and v_z . We note that stars at smaller R preferentially come from the higher L_z distribution and have a higher σ_z .

Fig. 2 shows the $z - v_z$ plane coloured by mean v_ϕ . Stars

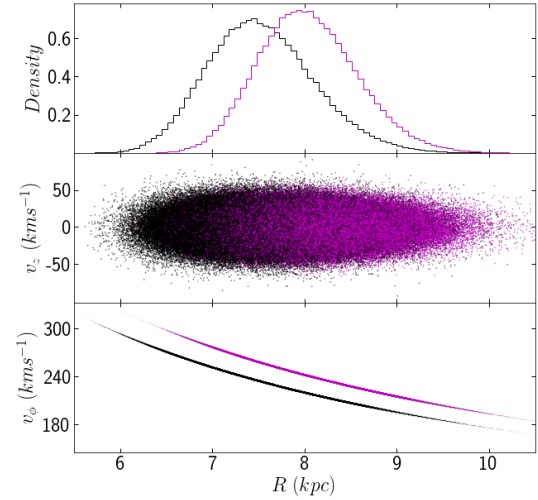


Figure 1. Properties of the initial conditions for the test-particle simulation described in Section 2.2.1. In the top panel we show a normalized histogram of the particle number as a function of R for populations 1 (black) and 2 (magenta), with a bin size of $\Delta R = 0.06 \text{ kpc}$. In the middle panel we show the distributions of stars in the two populations as a function of R and v_z while in the bottom panel we show distributions as a function of R and v_ϕ .

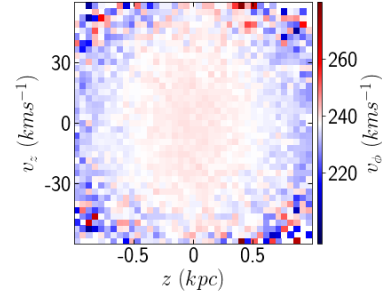


Figure 2. The $z - v_z$ plane colored by mean v_ϕ for the simulation described in Section 2.2.1. The bins have size $\Delta z = 0.05 \text{ kpc}$, and $\Delta v_z = 3 \text{ km s}^{-1}$. Bins with fewer than 10 particles are ignored.

at large radii in the $z - v_z$ plane, that is, stars with high E_z preferentially come from stars in population 1, which have lower v_ϕ , as seen in the bottom panel of Fig. 1.

The initial DF shown in Fig. 2 is perturbed by displacing it by 30 km s^{-1} in v_z . The particles are then evolved using a standard leap-frog algorithm for 300 Myr and the results are shown in Fig. 3. The number density shows the spiral pattern typical of phase wrapping. Stars orbit the $z - v_z$ plane in a clockwise sense and since those at large E_z have a lower vertical epicycle frequency, the DF quickly develops a trailing spiral. Also shown is the $z - v_z$ plane coloured by mean v_R and v_ϕ . Here, the pattern is essentially featureless, apart from the imprint of the number density distribution: With our separable potential the in-plane and vertical epicyclic motions completely decouple.

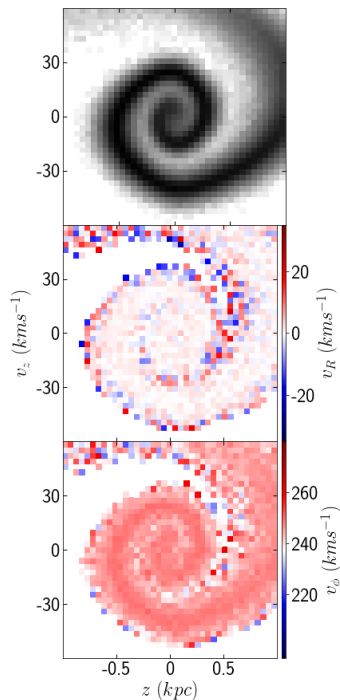


Figure 3. Number density and mean radial and azimuthal velocities in the $z - v_z$ plane for the toy model considered in Section 2.2.1 (toy model with additively separable potential). Top panel shows the number density. Bins in the middle and lower panels are coloured by v_R and v_ϕ , respectively. Bin sizes and particle number threshold are the same as in Fig. 2.

2.2.2 kinematic spirals in a coupled potential

Next we consider the addition of a $R - z$ term to the toy model potential:

$$\Phi(R, z) = \psi(R) + \chi(z) + \xi(R - R_s)z^2. \quad (10)$$

R_s is a constant radius characteristic of the distribution (If a Taylor expansion of the effective potential is performed for each L_z population, R_s is replaced by $R_c(L_z)$). For illustrative purposes, we choose $\xi = -0.24 \text{ Myr}^{-2} \text{ kpc}^{-1}$ and $R_s = 8 \text{ kpc}$. These values are consistent with the cubic terms that arise in realistic Milky Way potentials. The main effect of the new term is to introduce a linear dependence in R to the vertical epicyclic frequency. In particular the difference between the vertical frequency for a population 1 star with $R_c = 7.41 \text{ kpc}$ and a population 2 star with $R_c = 7.94 \text{ kpc}$ is 0.25 Myr^{-1} .

As before we sample an initial distribution (Eq. 3) with 500k particles, perturb it and integrate the perturbed distribution for 300 Myr. The results are shown in Figure 4. Not surprisingly, the spirals that appear in the $z - v_z$ number density distribution are virtually identical to the ones that appear in our separable model. However, the v_R and v_ϕ spirals are qualitatively different. In particular, there are gradients across the spiral arms and along their inner and outer edges. The addition of the $(R - R_s)z^2$ term implies a coupling between the in-plane and vertical epicyclic motions.

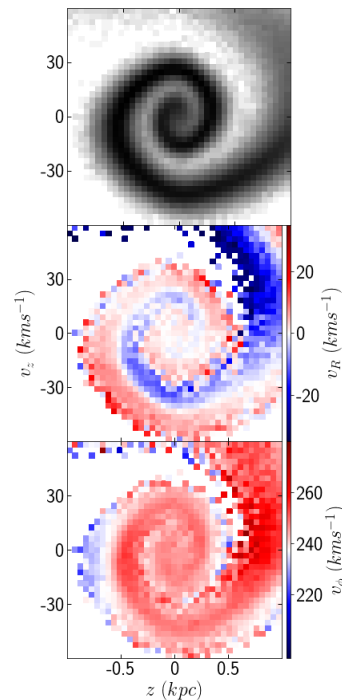


Figure 4. Same as Fig. 3 but for the model considered in Section 2.2.2 (toy model with $R - z$ coupling included in the potential).

2.3 Realistic Milky Way Potential

We conclude this section on test-particle simulations by considering a realistic Milky Way potential that comprises an exponential disc, an NFW halo (Navarro et al. 1997), and a Hernquist bulge (Hernquist 1990). We approximate the disc as a superposition of three Miyamoto-Nagai potentials (Miyamoto & Nagai 1975; Smith et al. 2015). The potential is similar to the MWPotential2014 model included with the GALPY code (Bovy 2015), but the specific model we used can be defined in GALPY using `HernquistPotential(a=0.035, amp=0.5)`, `MN3ExponentialDiskPotential(amp=7, hr=2.8/8, hz=0.3/8, sech=True)` and `NFWPotential(amp=5, a=1.4)`. The decomposition of the circular speed curve into the three components is shown in Fig. 5.

The results are shown in Fig. 6. The number density spiral is a bit more tightly wound than our previous example implying a stronger gradient in the vertical frequency with E_z . More striking are the differences between the v_R and v_ϕ spirals seen here and in our previous examples. In particular, there are now prominent gradients along the edges of the spirals. For example, along the inner edge of the v_ϕ spiral, the stars alternate between high azimuthal velocity (red) and low azimuthal velocity (blue) five times in a little over 360° . The fact that the variations in v_ϕ are strongest along the edges of the spirals makes sense since these stars have the largest E_z where the effect of the coupling term is the largest.

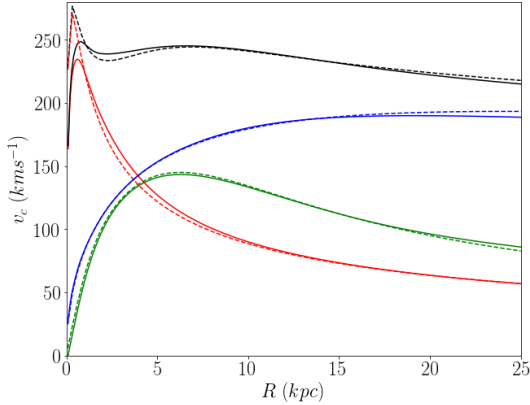


Figure 5. Circular speed curve for the Milky Way potential discussed in Section 2.3 (dashed curves) and self-consistent model discussed in Section 3 (solid curves). For each model we show the total circular speed (black curves) and contributions from the bulge (red) disk (green) and halo (blue).

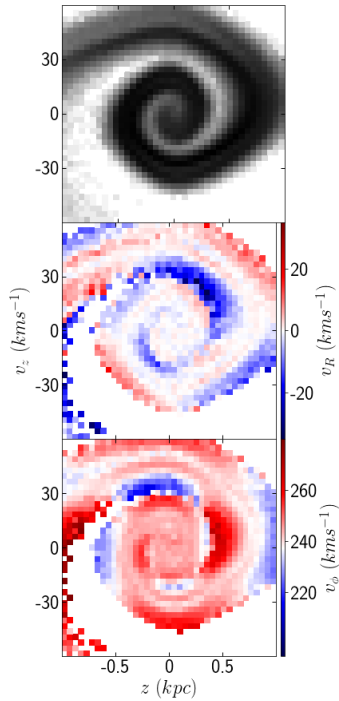


Figure 6. Same as Fig. 3 but for the model considered in Section 2.3 (realistic model for the Milky Way potential).

3 PHASE SPACE SPIRALS WITH SELF-GRAVITY

In the previous section, we considered test particles in a fixed axisymmetric potential. The evolution of their DF was therefore governed by kinematic phase mixing. Test particles were used by [de la Vega et al. \(2015\)](#) in their study of bending and breathing modes and by [Antoja et al. \(2018\)](#) and [Binney & Schoenrich \(2018\)](#) to explain the *Gaia* spirals. However, as stressed by [Hunter & Toomre \(1969\)](#) (see also [Sparke & Casertano \(1988\)](#)) there are two effects associated with a bending perturbation of a disc: the restoring force of the unperturbed disc on the perturbation and the

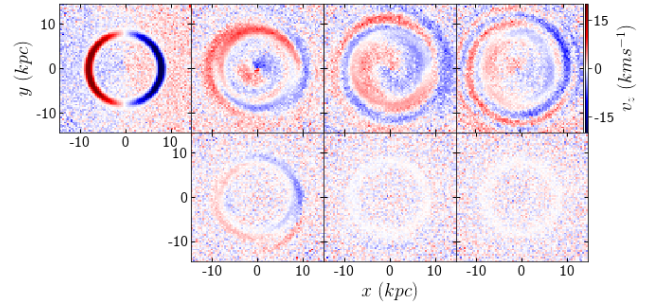


Figure 7. Face-on maps for the mean vertical velocity. Left-most top panel shows the initial conditions for both self-consistent and test-particle simulations. From left to right, one then has maps for the 250 Myr, 500 Myr, and 1 Gyr snapshots. The top row shows results for the self-consistent simulation while the bottom row shows results for the test particle simulation.

potential associated with the perturbation acting on the unperturbed disc. In effect, the test-particle models treat the former and ignore the latter. In linear perturbation theory, both effects enter at the same order. It follows that self-gravity will be important for the evolution of bending waves and phase space spirals.

In this Section we present results from simulations of a fully self-consistent disc-bulge-halo system. The initial conditions are generated with GALACTICS, which uses a disc DF given by Eq. 3 with $g(L_z)$ chosen to yield an exponential profile for the surface density (See [Kuijken & Dubinski \(1995\)](#); [Widrow et al. \(2008\)](#)). The model parameters are chosen so that the rotation curve decomposition into the three components matches the realistic Milky Way model introduced in the previous section, as shown in Fig. 5. We use 1M particles for the halo and 200K particles for the bulge. To boost mass resolution near the solar circle, we sample the region of the disc between 6.5 kpc and 9.5 kpc with 5M particles and the remainder with 1M particles. The particles in the ring then have a mass of about $1300 M_\odot$ or about 28 times less massive than the particles in the rest of the disc.

We introduce an *ad hoc* bend to the disc by applying a velocity perturbation to both low and high resolution disc stars of the form

$$\delta v_z = v_0 e^{-(R-R_0)^2/2\delta_R^2} \cos \phi \quad (11)$$

where we choose $v_0 = 30 \text{ km s}^{-1}$, $R_0 = 8 \text{ kpc}$, and $\delta_R = 500 \text{ pc}$. Thus, initially one side of the disc will bend to the North while the other will bend to the South.

The system is evolved for 1 Gyr with a timestep of 10^5 years and a Plummer softening of 50 pc. Face-on maps of the mean vertical velocity for the 250 Myr, 500 Myr, and 1 Gyr snapshots are shown in Fig. 7. In making this figure we reoriented the disc so that the direction corresponding to the smallest eigenvalue of the moment of inertia tensor and the angular momentum vector were normal to the plane of the map. Since the perturbation introduces a small angular momentum, when we reorient the disc, the region far from the perturbation is given a small z -velocity in the opposite sense of the perturbation, as seen, for example, in the upper-left panel.

To gain a handle on the effect self-gravity has on the

evolution of bending waves, we also follow the evolution of low and high resolution disc particles under the assumption that the background potential is fixed and given by the unperturbed potential of the model. The face-on maps of the mean vertical velocity are shown in Fig. 7. We see in the bottom three panels that the kinematic bending waves are rapidly damped, presumably due to phase mixing. By 500 Myr, the vertical velocity signal is entirely due to particle noise and, as one can clearly see in the figure, is significantly less in the annulus dominated by low mass particles. Conversely, in the upper panels we see that the bending waves persist with roughly constant amplitude through to 1 Gyr. Clearly, self-gravity is crucial to the persistence of bending waves in discs.

We next search for phase space spirals in a manner similar to what was done in Antoja et al. (2018) with GDR2. In particular, we select stars in a circular arc between 7.5 kpc and 8.5 kpc and over a range in ϕ that spans 1 rad. This region typically contains 250k particles, or about 1/20 of the total number of particles in our high-resolution ring. The number of stars here is thus a factor of 3 – 4 less than the number of stars in the arcs considered by Antoja et al. (2018). On the other hand, our arc is about five times wider in R and seven times wider in ϕ than the one they chose. Thus, even with our ring of low mass particles, our simulations have poorer particle and spatial resolution in comparison with the data.

The number counts and mean v_r and v_ϕ across the $z-v_z$ plane are shown in Fig. 8 and Fig. 9 for the same three snapshots that were used in Fig. 7. Spirals are found in both mean v_R and v_ϕ with an amplitude of $\sim 10 - 20 \text{ km s}^{-1}$, which is comparable to, though somewhat smaller than, the amplitude of the initial perturbation. As expected, the pattern winds up over time. In the v_ϕ panel of Fig. 1 from Antoja et al. (2018), one observes roughly one and a half wraps within $|z| < 700 \text{ pc}$. Our self consistent simulation appears to reach a comparable pattern around $t \simeq 1 \text{ Gyr}$, though by this time, the pattern is becoming difficult to discern.

The phase space spirals are more distinct in the test particle run. Indeed, a spiral pattern can be easily seen in the number counts, which is not the case in the self-consistent simulation. The degree of winding seen in the self-consistent and test-particle runs is fairly similar through the 500 Myr snapshot. However, by 1 Gyr, the test-particle run shows a tightly wound spiral with four phase space wrappings within $|z| < 1 \text{ kpc}$ while the self-consistent run shows about half that many.

The patterns seen in Figs. 9 and 8 as well as Fig. 7 can be understood as follows. In our test particle simulation, the evolution of the phase space DF is driven entirely by phase mixing in an analytic, time-independent, axisymmetric potential. It is therefore not surprising that over time, the DF develops intricate, fine-grained patterns such as those seen in the 1 Gyr panel of Fig. 9. These patterns are typically washed out when one maps moments of the DF, as in Fig. 7. By contrast, when self-gravity is included, the disc develops persistent vertical oscillations, as seen in Fig. 7, that is roughly constant between 500 Myr and 1 Gyr. The spiral pattern seen in the 1 Gyr panel of Fig. 8 may well be a manifestation of these persistent oscillations.

Two effects may explain why the spirals in our self-consistent simulation are less well-defined than in the test-

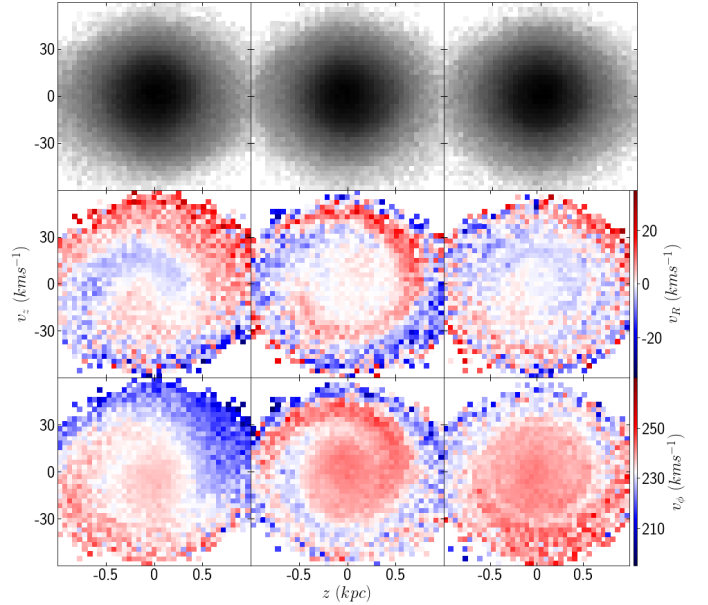


Figure 8. Number density and mean v_R and v_ϕ maps for the self-consistent simulation. Each row has the same format as in figures in Section 2. From left to right, the columns are for the 250 Myr, 500 Myr, and 1 Gyr snapshots.

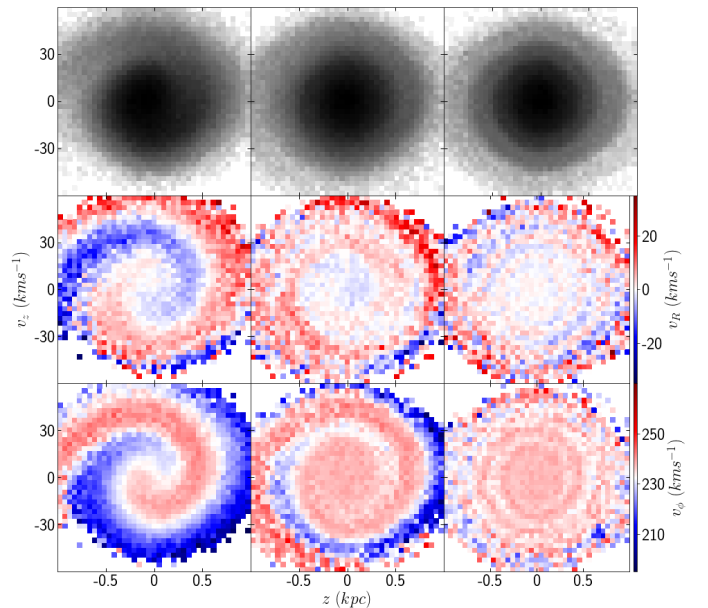


Figure 9. Same as Fig. 8 but for the test particle simulation.

particle case. First, the disc in the self-consistent simulation can develop non-axisymmetric features, such as spiral structures, in addition to the features that arise from the initial perturbation. Thus, the particles that end up in the circular arc used in Fig. 8 will have been subjected to a more complicated forcing function than those in the test-particle run. Second, particles in the self-consistent run experience two-body relaxation effects not present in our test-particle simulation. However, the two-body relaxation time for the

disc is longer than the duration of the simulation by several orders of magnitude. We also note that additional simulations indicate that our results are relatively insensitive to choice of softening length and time-step. Nevertheless, no N-body simulation is perfectly collisionless. The combination of these effects may explain why the spiral patterns that arise when including self gravity are not as well-defined as those with test particles.

4 CONCLUSIONS

In this paper we have focused on three facets of phase space spirals. First, spirals similar to those found in *Gaia* DR2 naturally arise when the disc experiences a bending perturbation. In general, a passing satellite will cause the disc to bend (Toth & Ostriker 1992; Sellwood et al. 1998; Widrow et al. 2014; Binney & Schoenrich 2018), and within a few dynamical times these bends lead to spirals in the $z - v_z - v_R - v_\phi$ space. Second, the non-separable nature of the effective potential is crucial for understanding the morphology of the spirals. This effect, which appears at cubic and higher order in the Taylor expansion of the effective potential, implies a coupling of the in-plane and vertical epicyclic motions and leads to variations in v_R and v_ϕ across and along the edges of the spirals. Finally, self gravity appears to be an essential ingredient in any study of bending waves in discs.

The results from our toy-model simulations suggest that by studying the morphology of phase space spirals, we can probe the detailed structure of the Galactic potential. In particular, one might gain a handle on the coefficients of cubic and quartic terms in the Taylor expansion of the effective potential near the Sun and beyond, once future data releases from *Gaia* become available.

The natural way forward is to test these ideas with different models for the Galactic potential. Studies of this type will allow us to determine just how sensitive the phase space spirals are to the potential. Such a program should be straightforward to accomplish with kinematic models where test particles are used as probes. However, our self-consistent simulations suggest that these models may miss the essential physics of self-gravity in the perturbed disc. Unfortunately, self-consistent simulations are computationally expensive, and the mass and spatial resolution that can be achieved, especially if one aims to study a large parameter space, are well below the resolution available in the data.

ACKNOWLEDGMENTS

We thank Jo Bovy for help with the Galactic potential used in Section 2. This work was supported by a Discovery Grant with the Natural Sciences and Engineering Research Council of Canada.

REFERENCES

Antoja T., et al., 2018, preprint ([arXiv:1804.10196](https://arxiv.org/abs/1804.10196))
 Bennett M., Bovy J., 2018, *MNRAS*, 482, 1417
 Binney J., 1992, *ARA&A*, 30, 51
 Binney J., Schoenrich R., 2018, preprint ([arXiv:1807.09819](https://arxiv.org/abs/1807.09819))

Binney J., Tremaine S., 2008, *Galactic Dynamics: Second Edition*. Princeton University Press
 Bovy J., 2015, *ApJS*, 216, 29
 Carlin J. L., et al., 2013, *ApJ*, 777, L5
 Chequers M. H., Widrow L. M., 2017, *MNRAS*, 472, 2751
 Chequers M. H., Widrow L. M., Darling K., 2018, preprint ([arXiv:1805.12449](https://arxiv.org/abs/1805.12449))
 Debattista V. P., 2014, *MNRAS*, 443, L1
 Feldmann R., Spolyar D., 2015, *MNRAS*, 446, 1000
 Gaia Collaboration et al., 2018b, preprint ([arXiv:1804.09380](https://arxiv.org/abs/1804.09380))
 Gaia Collaboration Brown A. G. A., Vallenari A., Prusti T., de Bruijne J. H. J., Babusiaux C., Bailer-Jones C. A. L., 2018a, preprint ([arXiv:1804.09365](https://arxiv.org/abs/1804.09365))
 Gómez F. A., Minchev I., O’Shea B. W., Beers T. C., Bullock J. S., Purcell C. W., 2013, *MNRAS*, 429, 159
 Gómez F. A., White S. D. M., Grand R. J. J., Marinacci F., Springel V., Pakmor R., 2017, *MNRAS*, 465, 3446
 Hernquist L., 1990, *ApJ*, 356, 359
 Hunter C., Toomre A., 1969, *Dynamics of the Bending of the Galaxy*. p. 747, [doi:10.1086/149908](https://doi.org/10.1086/149908)
 Kuijken K., Dubinski J., 1995, *MNRAS*, 277, 1341
 Kuijken K., Gilmore G., 1989, *MNRAS*, 239, 571
 Miyamoto M., Nagai R., 1975, *PASJ*, 27, 533
 Monari G., Famaey B., Siebert A., 2015, *MNRAS*, 452, 747
 Navarro J. F., Frenk C. S., White S. D. M., 1997, *ApJ*, 490, 493
 Schönrich R., Dehnen W., 2018, *MNRAS*, 478, 3809
 Sellwood J. A., 2013, *Dynamics of Disks and Warps*. p. 923, [doi:10.1007/978-94-007-5612-0_18](https://doi.org/10.1007/978-94-007-5612-0_18)
 Sellwood J. A., Nelson R. W., Tremaine S., 1998, *ApJ*, 506, 590
 Smith R., Flynn C., Candlish G. N., Fellhauer M., Gibson B. K., 2015, *MNRAS*, 448, 2934
 Sparke L. S., Casertano S., 1988, *MNRAS*, 234, 873
 Toth G., Ostriker J. P., 1992, *ApJ*, 389, 5
 Widrow L. M., Pym B., Dubinski J., 2008, *ApJ*, 679, 1239
 Widrow L. M., Gardner S., Yanny B., Dodelson S., Chen H.-Y., 2012, *ApJ*, 750, L41
 Widrow L. M., Barber J., Chequers M. H., Cheng E., 2014, *MNRAS*, 440, 1971
 Williams M. E. K., et al., 2013, *MNRAS*, 436, 101
 Xu Y., Newberg H. J., Carlin J. L., Liu C., Deng L., Li J., Schönrich R., Yanny B., 2015, *ApJ*, 801, 105
 Yanny B., Gardner S., 2013, *ApJ*, 777, 91
 de la Vega A., Quillen A. C., Carlin J. L., Chakrabarti S., D’Onghia E., 2015, *MNRAS*, 454, 933

This paper has been typeset from a $\text{\TeX}/\text{\LaTeX}$ file prepared by the author.